



# A Numerical and Field Investigation of Surface Heat Fluxes from Small Wind-Sheltered Waterbodies in Semi-Arid Western Australia

M.R. HIPSEY, M. SIVAPALAN and T.P. CLEMENT\*

*Centre for Water Research, University of Western Australia, 35 Stirling Hwy, Crawley, Western Australia, 6009*

Received 6 September 2002; accepted in revised form 14 May 2003

**Abstract.** Shelterbelts are used for a variety of purposes in agricultural environments, primarily because of their ability to improve the downwind microclimate. Excessive evaporative losses from small, agricultural water supply reservoirs in semi-arid Western Australia motivated a combined numerical modelling and field investigation into the potential for using shelterbelts to reduce evaporation from these open waterbodies. A numerical model of the disturbed momentum and turbulence fields in the region modified by the wind-shelter was employed and accounted for the presence of a waterbody downwind. The model was coupled with conservation equations for heat and moisture and sensible and latent heat fluxes were estimated from the simulated momentum, temperature and humidity fields. The numerical simulations were tested against four days of field data from two experiments conducted in the agricultural districts of southwest Western Australia that measured boundary-layer evolution over a variety of small waterbodies protected by artificial and natural wind-shelters. The model provided good predictions of windspeed during neutral conditions, but inadequate specification of the upwind boundary during non-neutral stabilities resulted in the model failing to capture any sensitivity to atmospheric stability as seen in the field data. Despite this limitation, the temperature and humidity fields were adequately captured by the model, and evaporative mass flux predictions also agreed well with estimates taken from water-balance measurements. It is concluded that well-designed wind-shelters can reduce evaporation from open waterbodies by 20–30% as a result of reductions in the velocity scales responsible for removing moisture from the water surface. The model can be used to estimate the values of various shelterbelt design parameters (e.g., porosity, height) that could be applied in the field to provide optimum evaporation reductions.

**Key words:** evaporation reduction, microclimate, numerical model, shelterbelt, surface heat flux, windbreak

## 1. Introduction

Shelterbelts have long been used for their environmental benefits, such as reducing wind-induced erosion and crop damage, and for improving the downwind microclimate experienced by crops and livestock. These outcomes result primarily from a reduction in the mean windspeed for some distance downwind of the shelter. Recently, a new application has gained interest in the semi-arid regions of Western

\*Now at Department of Civil Engineering, Auburn University, AL 36830 U.S.A.

Australia, where shelterbelts have been employed in an effort to reduce evaporation from rural water stores. This investigation examines how modifications to the flow field and microclimate brought about by the presence of a wind-shelter influence surface heat transfer, and hence evaporation, from small waterbodies situated downwind.

Understanding modifications to the microclimate leeward of wind-shelters has been an active area of research for several decades. The primary impetus for this research has been to understand how the changes in microclimate impact crop productivity, particularly through changes to evaporation from bare soil and transpiration from the crops themselves. For example, Rosenberg [1] and Brown and Rosenberg [2] found that vapour pressure and air temperature were, on average, increased above an irrigated crop protected by a shelterbelt, and that the magnitude of the vapour pressure difference varied as a function of distance downwind. Lomas and Schlesinger [3], Skidmore and Hagen [4] and Messing *et al.* [5] documented that shelterbelts reduced evaporation in proportion to the windspeed reduction, and reported evaporation reductions of the order of 35% based on direct evaporation measurements. McNaughton [6] summarizes that these modifications are a result of reduced turbulent transfer in the quiet zone directly behind the shelter, which allows accumulation of moisture near the surface and therefore reduces the vapour pressure gradient driving the evaporative heat flux. Further downwind in the turbulent wake zone, the flow recovers to upwind conditions and enhanced turbulence intensity implies that the reverse is true. This argument was recently weakened by Cleugh and Hughes [7] who suggested that velocity variances are not increased in the wake zone, and that scalar concentrations tend to just return to their upwind values. Turbulence flux estimates by Prueger *et al.* [8] however, indicated an increase in latent heat flux at all regions downwind of a shelter during low wind conditions. Exceptions were also reported by Skidmore *et al.* [9] and Brenner *et al.* [10].

The efficiency of wind-shelters in modifying the downwind windspeed and microclimate is dependent on many factors, including shelterbelt height and porosity, upwind surface roughness and atmospheric stability. Although there is a significant body of literature that contributes to a broad understanding of the role of each of these factors, the conclusions are often specific to a unique field environment where a specific factor was studied by fixing other conditions that would influence the result. From an experimental point of view, this is necessary to isolate the relevant process but it makes extrapolation of results to a predictive capacity difficult, particularly for complicated field scenarios such as that described here, where several factors vary concurrently. More recently, enhanced computer power has enabled the development of complex numerical models that assist in deciphering the complexities associated with turbulent wake flows in the natural environment, although, progress has been slow as a complete treatment requires solution of the full turbulent Navier–Stokes equations.

Early work on the numerical modelling of flow about a shelterbelt was conducted by Durst and Rastogi [11] who simulated solid barriers, and Hagen *et al.*

[12] who allowed for porous barriers. A comprehensive modelling effort was later conducted by Wilson [13] who experimented with various turbulent closure models and managed to reproduce many features of the momentum field seen in the experimental data collected by Bradley and Mulhearn [14], although in all the simulations, the model underestimated over-speeding above the barrier and the leeward velocity recovery. A decade later, Wang and Takle [15] hypothesized that the underestimation was due to the parameterization of the shelter (at least for natural shelterbelts), and instead performed a phase-averaging of the equations of motion to explicitly capture the force imposed on the flow by the shelter [16, 17]. This was reported to more accurately capture the speed-up zone over the barrier, the recovery rate in the far lee and the re-circulation observed in the immediate lee of dense shelters, although some uncertainty exists as to whether the improvement was due to a difference in the shelterbelt parameterization or the numerical method used in the analysis [18, 19]. More recently, a multiple shelterbelt network was successfully modelled using large-eddy simulation techniques [20].

Despite growing confidence in the numerical models that simulate the aerodynamic behavior of wind-shelters, models of microclimate response to the altered flow fields are still in their infancy. Wang and Takle [21] coupled their aerodynamic model with a resistance formulation of soil-vegetation-atmosphere processes to describe persistent spatial and temporal patterns in downwind latent and sensible heat fluxes. They found that the shelter effect on evapotranspiration was largely controlled by water availability, as well as the degree of flow separation. To the best of our knowledge, the first effort to incorporate transport of a scalar was completed by Patton *et al.* [20] whose large-eddy simulation demonstrated how the protection afforded by the shelterbelt modified downstream scalar concentrations. Recently, Wilson *et al.* [22] applied a modified Rao–Wyngaard–Cote aerodynamic model with a higher-order turbulent closure that also solved the full conservation equations for heat and a scalar [23, 24]. However, this model was individually applied to predict internal boundary layer development over a non-sheltered waterbody and to predict the modification to the flow-fields brought about by the presence of a shelterbelt, but insufficient experimental data prevented these two scenarios being brought together into a single simulation.

It is the objective of this paper to present a combined field and modelling approach to gain insights into surface heat fluxes from small waterbodies protected from the wind. A two-dimensional (2D) numerical model was developed using an approach similar to that of Wang and Takle [15], with extensions to include the presence of the waterbody and the disturbed heat and moisture fields. The model was applied to a complicated field scenario where wind-shelters have been situated upwind of small rural dams. This situation differs from the idealized conditions assumed in previous published investigations for three main reasons: (1) The wind is subject to significant roughness changes as it passes from land to water and back to land again; (2) the different surface heat fluxes on the windward and leeward sides of the shelter introduce alongwind gradients in atmospheric stability; and (3)

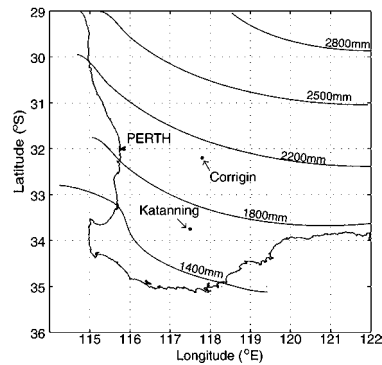


Figure 1. Location of field sites in southern Western Australia. Contours indicate average annual Class-A pan evaporation (data taken from Agriculture Western Australia database).

the waterbody itself is dynamic and can respond to surface forcing. The former two factors are both known to influence the velocity recovery downwind of a shelter, but have yet to be included in any modelling effort. The initial focus of this study is therefore to present a model capable of simulating surface heat transfer from waterbodies protected from the wind and to validate model predictions with data taken from a comprehensive field experiment conducted in southwest Western Australia where boundary layer evolution was monitored over several small, wind-sheltered waterbodies. This systematic analysis allows us to gain insights into the mechanisms through which shelter modifies surface heat transfer. Finally, we use the model results and field data to illustrate the ability of wind-shelters to reduce evaporation from small water supply reservoirs.

## 2. Field Experiment

The field experiment was conducted at two locations, each with three similar sized waterbodies, in the wheatbelt of southern Western Australia (Figure 1). The first site was located at Corrigin on a cereal and sheep farm that experiences a mean annual rainfall of 375 mm and an average annual potential evaporation (Class-A pan) of 2100 mm. The second site was located at Katanning, 200 km south of Corrigin and 350 km southeast of Perth, with a mean annual rainfall of 450 mm and an average annual potential evaporation of 1800 mm.

The field trial conducted at Corrigin ran between 9th September 2000 and 24th November 2000, and the Katanning trial ran between 26th November 2000 and 9th January 2001. The period between October and March in southwest Western Australia is typically hot and dry due to the easterly and north-easterly winds bringing air across the desert. This period is of most interest from a water conservation perspective because of the very large evaporation rates.

## 2.1. SHELTER SCENARIOS

Three waterbodies at each field location were chosen for experimentation, and were subject to different degrees of sheltering from the wind. The chosen waterbodies were typical square prismoidal earth reservoirs with water surface areas of approximately 3600 m<sup>2</sup> (waterbody length,  $X_W = 60$  m), and maximum depths ranging between 4 and 6 m. The reservoirs at both sites are surrounded on three or four sides by solid earth banks that rise to a height of 1.5 m. The three waterbodies on both sites were chosen to minimize differences between shape and size, as well as upwind topography and land-use differences, so that the approaching flow and waterbody dynamics were similar in all cases. The three reservoirs at each site are differentiated as follows (Figure 2a):

**BO** Bank Only – mostly unprotected from the wind except for some small protection provided by the bank ( $X_W/H_{BO} = 40$ , where  $H_{BO}$  is the height of the upwind bank);

**AB** Artificial Barrier – similar to BO but with a 2.5 m shadecloth barrier (30% porosity) erected on two sides (see below) aligned to catch the warm, dry summer winds ( $X_W/H_{AB} = 15$  where  $H_{AB}$  is the height of the upwind bank plus the height of the barrier), and;

**NS** Natural Shelterbelt – the waterbody was located downwind of a natural tree shelterbelt consisting of Eucalypt species, with optical porosity of approximately 50% and a height of 8 m and 15 m for Katanning ( $X_W/H_{NS} = 7.5$ ) and Corrigin ( $X_W/H_{NS} = 4$ ), respectively.

The application of a two-dimensional aerodynamic model to these scenarios meant that it was important to minimize three-dimensional ‘edge effects’ in the field. For both the Corrigin and Katanning NS scenarios this did not present a problem as the shelterbelts laterally extended some distance beyond the edges of the waterbody. In addition, the earthen banks along the side of the waterbodies provide some protection from lateral wind motions. For the AB scenario however, the lateral extent of the barrier was only slightly beyond the edges of the waterbody. This problem was overcome by constructing the barrier also along one side. Based on the predominant wind direction it was deemed unnecessary to construct it along the other side. As with the NS scenarios, the earthen banks along the side also provide protection from lateral wind gusts.

## 2.2. INSTRUMENTATION

The monitoring equipment installed at each reservoir consisted of an upwind station measuring wind speed and direction, air temperature, humidity and solar radiation (at 2 m), plus three floating platforms distributed across the water surface

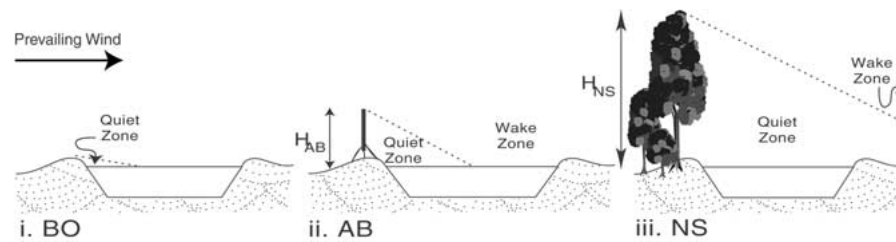


Figure 2a. Field schematic showing the three experimental scenarios: i. Bank Only (BO), ii. Artificial Barrier (AB), iii. Natural Shelter (NS).

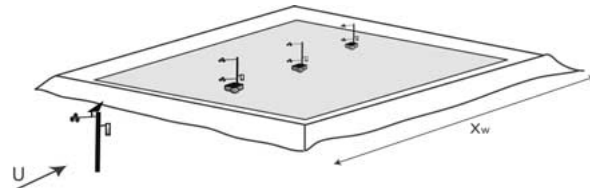


Figure 2b. Oblique view of the BO scenario.

(Figure 2b). The floating platforms measured the temperature of the surface waters and supported a 2 m high mast with cup anemometers at 0.5 m and 2.0 m (Figure 2c). One or two of the platforms during each of the trials also measured air temperature and relative humidity 0.5 m above the surface. All of the instruments scanned data every 12 s, and recorded the average every 15 min. The instrumentation and float locations for each of the study sites are presented in Table I.

Evaporation from each waterbody was estimated using a water-balance approach. The change in water-depth of the reservoirs was measured using a vented and temperature compensated pressure sensor placed on the reservoir floor, and depth evolution was disaggregated into seepage and evaporation components by

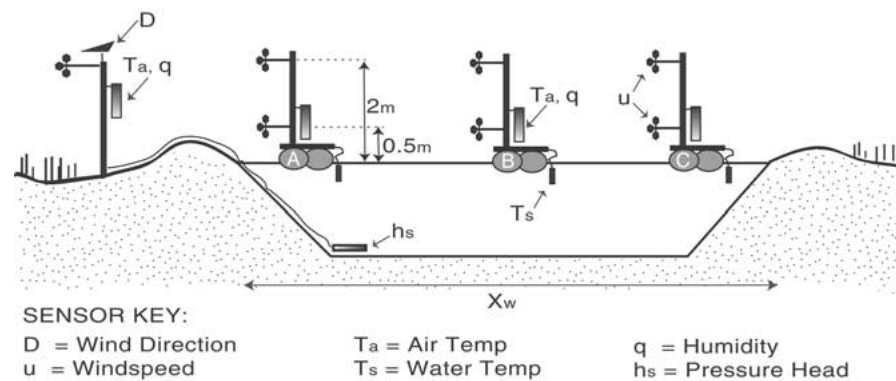


Figure 2c. Instrumentation schematic for the BO scenario. The AB and NS scenarios were otherwise the same except for the presence of the wind-shelter.

Table I. Monitoring equipment and float locations for the Corrigin 14–15th November 2000) and Katanning (27–28th November 2000) field trials. Floats A, B and C correspond to the locations shown in Figure 2c. The instrumentation used included windspeed and direction ( $u$  and  $D$ ), solar radiation ( $\phi_K$ ), air temperature ( $T_a$ ), humidity ( $q$ ) and surface water temperature ( $T_s$ ). The subscripts denote the height in metres the instrument was set above the surface.

Station	Instrument	Corrigin			Katanning		
		BO	AB	NS	BO	AB	NS
Upwind	$u_2$	•	•	•	•	•	•
	$D_2$	•	•	•	•	•	•
	$T_{a2}$	•	•	•	•	•	•
	$q_2$	•	•	•	•	•	•
	$\phi_{K2}$	•	•		•		
Float A	$x/H$	2.5	3.0	2.0	4.0	3.5	3.0
	$u_2$	•	•	•	•		•
	$D_2$				•		•
	$u_{0.5}$	•	•	•	•		•
	$T_{a0.5}$	•	•				•
	$q_{0.5}$	•	•				•
	$T_s$	•	•	•	•	•	•
Float B	$x/H$	7.2	8.0	2.5	9.1	7.0	N/A
	$u_2$		•	•	•	•	
	$D_2$		•	•			
	$u_{0.5}$		•	•	•	•	
	$T_{a0.5}$			•		•	
	$q_{0.5}$			•		•	
	$T_s$	•	•	•		•	
Float C	$x/H$	14.5	14.0	2.9	15.0	12.5	6.6
	$u_2$		•		•	•	
	$D_2$						
	$u_{0.5}$		•		•	•	
	$T_{a0.5}$		•		•		
	$q_{0.5}$		•		•		
	$T_s$	•	•	•	•	•	•

identifying periods of little or no evaporation, and then assuming changes in storage were solely attributable to leakage (livestock were excluded during these periods and no rainfall or runoff occurred). The seepage rate was considered a Darcy flux, linearly related to the measured pressure head, so that the seepage rate was calculated as a function of time, and therefore subtracted from the depth trace to leave a time series of depth change responding solely due to evaporative losses. To minimize the significance of random and measurement errors introduced through this method, the evaporation data were integrated over a daily period before comparison with the model results.

### 3. Numerical Model

#### 3.1. THEORY

The mathematical model used for predicting flow through a porous barrier is based on that of Wang and Takle [15], subsequently referred to as the ‘WT’ model. This approach was chosen because their work was intended specifically for natural shelterbelts and has been used to examine a variety of shelterbelt design parameters (see [25], for an overview).

Under the Boussinesq assumption for compressible flow, the unsteady Reynolds averaged equations of motion for a 2D turbulent flow through a natural shelterbelt reduce to [17]:

$$\frac{\partial u}{\partial t} + \frac{\partial u}{\partial x} + x \frac{\partial u}{\partial z} = -\frac{1}{\rho_0} \frac{\partial p}{\partial x} - \frac{\partial \overline{u^2}}{\partial x} - \frac{\partial \overline{u'w'}}{\partial z} - C_D A U u, \quad (1)$$

$$\frac{\partial w}{\partial t} + w \frac{\partial w}{\partial z} + u \frac{\partial w}{\partial x} = g \frac{\hat{\theta}}{\theta_0} - \frac{1}{\rho_0} \frac{\partial p}{\partial z} - \frac{\partial \overline{w^2}}{\partial z} - \frac{\partial \overline{u'w'}}{\partial x} - C_D A U w, \quad (2)$$

$$\frac{\partial u}{\partial x} + \frac{\partial w}{\partial z} = 0, \quad (3)$$

where  $u$  and  $w$  are mean velocities in the horizontal,  $x$ , and vertical,  $z$ , directions,  $u'$  and  $w'$  are their respective fluctuating components and  $p$  is dynamic pressure. Because we are only concerned with the shallow atmospheric surface layer, equation (2) is nonhydrostatic but accounts for thermally induced changes in density through the first term on the right hand side; here,  $\hat{\theta}$  is the local potential temperature departure from the reference temperature,  $\theta_0$ . The last term on each of the momentum equations represents the drag force imposed on the flow as it passes through the shelter, where  $C_D$  is the drag coefficient for unit plant area density,  $A$  is the plant area density and  $U = \sqrt{u^2 + w^2}$  is the mean windspeed.

As with the WT model, we use a gradient-diffusion closure scheme making it similar in application to commonly used  $K - E - \epsilon$  turbulence models. Based on this approach, the Reynolds stress terms are parameterized as:

$$-\overline{u'w'} = K_M \left( \frac{\partial u}{\partial z} + \frac{\partial w}{\partial x} \right), \quad (4)$$

$$-\overline{u'^2} = K_M \left( \frac{\partial u}{\partial x} - \frac{\partial w}{\partial z} \right) - \frac{2}{3}E, \quad (5)$$

$$-\overline{w'^2} = K_M \left( \frac{\partial w}{\partial z} - \frac{\partial u}{\partial x} \right) - \frac{2}{3}E, \quad (6)$$

where  $K_M = c_1 l \sqrt{E}$  is the eddy viscosity,  $E = 1/2 \sqrt{u'^2 + w'^2}$  is the turbulent kinetic energy (TKE) and  $l$  is the master length scale of the turbulence. The use of 'K-theory' for this application has been justified by Wilson [13] and Wang and Takle [15], who found only marginal improvement in prediction of the mean flow field through use of higher order closure models. To close the equation set (1–6), conservation equations for  $E$  and then  $El$  are solved [26, 27],

$$\begin{aligned} \frac{\partial E}{\partial t} + u \frac{\partial E}{\partial x} + w \frac{\partial E}{\partial z} = \frac{\partial}{\partial x} \left( K_E \frac{\partial E}{\partial x} \right) + \frac{\partial}{\partial z} \left( K_E \frac{\partial E}{\partial z} \right) + K_M \left[ \left( \frac{\partial u}{\partial z} + \frac{\partial w}{\partial x} \right)^2 \right. \\ \left. + 2 \left\{ \left( \frac{\partial u}{\partial x} \right)^2 + \left( \frac{\partial w}{\partial z} \right)^2 \right\} \right] - \beta g \overline{w'\theta'_V} - c_2 \frac{E^{3/2}}{l} + C_D A U^3, \end{aligned} \quad (7)$$

$$\begin{aligned} \frac{\partial El}{\partial t} + u \frac{\partial El}{\partial x} + w \frac{\partial El}{\partial z} = \frac{\partial}{\partial x} \left( K_E \frac{\partial El}{\partial x} \right) + \frac{\partial}{\partial z} \left( K_E \frac{\partial El}{\partial z} \right) + c_3 l K_M \\ \left[ \left( \frac{\partial u}{\partial z} + \frac{\partial w}{\partial x} \right)^2 + 2 \left\{ \left( \frac{\partial u}{\partial x} \right)^2 + \left( \frac{\partial w}{\partial z} \right)^2 \right\} \right] - \beta g \overline{w'\theta'_V} - c_2 \frac{E^{3/2}}{l} + C_D A U^3. \end{aligned} \quad (8)$$

Here  $K_E$  is the transport coefficient of TKE, and is linearly related to the transport coefficient of momentum such that  $K_E = c_0 K_M$ . The constants  $c_0 - c_5$  have been determined experimentally in simple flows where the material derivative was assumed negligible (i.e., where a local production-dissipation balance exists in the flow), and have since been used successfully in a wide range of geophysical flows [26].

The WT model has been extended to account for vertical stratification through inclusion of a buoyancy production term in both (7) and (8); here  $\beta$  is the coefficient of thermal expansion,  $g$  is acceleration due to gravity and  $w'\theta'_V$  is the vertical turbulent flux of heat. The subscript V denotes the use of virtual potential temperature, defined as:

$$\theta_V = \left( \frac{p}{p_0} \right)^{R/c_p} (1 + 0.61q) (T + 273.15), \quad (9)$$

where  $\theta_V$  is in degrees Kelvin and  $T$  is temperature in degrees Celsius,  $q$  is specific humidity,  $R$  is the universal gas constant and  $c_p$  is specific heat at constant pressure. We parameterize the vertical heat flux as:

$$-\overline{w'\theta'_V} = K_H \frac{\partial \theta_V}{\partial z}, \quad (10)$$

where  $K_H$  is the eddy transport coefficient of heat, and is related to the eddy viscosity by the turbulent Prandtl number,  $Pr_T = K_M/K_H$ .

By assuming that the turbulence is isotropic, the evolving temperature and humidity fields are solved using conservation equations for the transport of heat and moisture using parameterizations similar to (10):

$$\frac{\partial \theta}{\partial t} + u \frac{\partial \theta}{\partial x} + w \frac{\partial \theta}{\partial z} = \frac{\partial}{\partial z} \left( K_H \frac{\partial \theta}{\partial z} \right) + \frac{\partial}{\partial x} \left( K_H \frac{\partial \theta}{\partial x} \right) + \frac{\phi_H}{c_p \rho}, \quad (11)$$

$$\frac{\partial q}{\partial t} + u \frac{\partial q}{\partial x} + w \frac{\partial q}{\partial z} = \frac{\partial}{\partial z} \left( K_q \frac{\partial q}{\partial z} \right) + \frac{\partial}{\partial x} \left( K_q \frac{\partial q}{\partial x} \right) + \frac{\phi_E}{\lambda_E \rho}, \quad (12)$$

where  $K_q$  is the moisture equivalent to  $K_H$ . The source terms on the right hand side account for sensible and latent heat fluxes respectively,  $\phi_H$  and  $\phi_E$ , from the waterbody and are calculated according to:

$$\phi_H = \rho c_p \overline{w'\theta'}, \quad (13)$$

$$\phi_E = \rho \lambda_E \overline{w'q'}, \quad (14)$$

where  $\lambda_E$  is the the latent heat of evaporation. The kinematic heat flux,  $\overline{w'\theta'}$ , over the surface is governed by the local friction velocity,  $u_*$ , and temperature scale,  $\theta_*$ , such that  $\overline{w'\theta'} = -u_*\theta_*$ , where  $\theta_*$  reflects the temperature gradient immediately above the surface:

$$\theta_* = \frac{\theta_{j=1} - \theta_s}{\ln(z_{j=1}/z_{0h})}. \quad (15)$$

Here,  $j = 1$  denotes the first grid point from the surface,  $\theta_s$  is the surface water temperature and  $z_{0h}$  is the temperature roughness length. Analogous expressions were used to calculate the surface kinematic moisture flux,  $\overline{w'q'}$ .

Additionally, the shelter itself is assumed to not participate in the balances of heat and moisture. This is justified for this application as the shelterbelts used in Western Australia are typically sclerophyllous, and have limited interaction with the atmosphere owing to high stomatal regulation (i.e., closure) during dry conditions. In any event, these reservoirs leak considerably and so the water accessed by trees is already lost from the water store.

### 3.2. NUMERICAL IMPLEMENTATION

For consistency, we used a numerical method similar to the WT model (see also [18, 19]). Rather than solely documenting the differences and additions, we have

provided a brief overall summary of the numerical scheme so that this may be used as a stand-alone methodology.

### 3.2.1. Computational Domain and Solution Technique

The computational domain ranged from 30H upwind to a minimum of 100H downwind of the shelter and spanned 8H in the vertical, where H is the height of the shelter. The grid spacing was regular in the vertical and set at a constant 0.1H. Variable grid spacing was used in the horizontal, with higher resolution near the shelterbelt to minimize error where gradients were expected to be steep. The spacing ranged from 0.5H between the upwind boundary and  $x = -2H$ ; 0.25H on either side of the shelter; 0.15H within the the region of the shelter; and 0.5H to the downstream boundary (Figure 3).

The momentum equations (1 and 2), continuity equation (3), turbulence equations (7, and 8), and heat and moisture equations (11 and 12), were subject to the finite difference method (upstream differencing for the advection terms, forward differencing for the time terms and centred differencing for the pressure terms) using a fully-implicit scheme with Picard linearization. The resultant set of linear algebraic equations was arranged into tri-diagonal matrices and sequentially solved using an Alternating Direction Implicit (ADI) scheme. To account for the dynamic pressure gradients, we use the projection method [28], which, in the first step, solves for provisional velocity fields,  $u^*$  and  $w^*$ , by dropping the pressure gradient terms out of the momentum equations. The provisional velocity fields are then related to continuity-satisfying velocity fields following:

$$u^{n+1} = u^* - \frac{\Delta t}{\rho_o} \frac{\partial p}{\partial x} \quad (16)$$

$$w^{n+1} = w^* - \frac{\Delta t}{\rho_o} \frac{\partial p}{\partial z} \quad (17)$$

where  $n$  is the current timestep. By taking the divergence of (16) and (17), we obtain the Poisson equation:

$$\nabla^2 \frac{p}{\rho_o} = \frac{1}{\Delta t} \left( \frac{\partial u^*}{\partial x} + \frac{\partial w^*}{\partial z} \right). \quad (18)$$

Equation (18) was solved using successive over-relaxation with an overrelaxation factor of 1.75 and a convergence criterion of  $10^{-4} \text{ m}^2 \text{ s}^{-2}$  to obtain the  $n + 1$  pressure field. As with the WT code, we also note that computational accuracy of the pressure field was a key condition in minimising error over long time integrations. Although the equations include unsteady terms, the model was run with constant forcing for each simulation to obtain a steady solution for the particular set of forcing parameters.

### 3.2.2. Boundary and Initial Conditions

3.2.2.1. *Momentum Fields.* Initially we imposed a logarithmic profile based on upwind windspeed data, with  $w$  and  $p$  set everywhere to 0,  $E = 6.6u_*^2$  and  $El = kzE$ , where  $k$  is von Karman's constant. Because of the variable surface forcing in the alongwind direction, the model was run without a shelterbelt to allow the internal boundary layers associated with the roughness, temperature and moisture changes to fully develop. Once a stationary solution was reached, the shelterbelt was 'turned on'.

At the inflow boundary, the horizontal velocity was held at the logarithmic value reached after the 'spin-up' period, as were the values for  $E$  and  $El$ . The vertical velocity,  $w$ , was set to zero for all  $z$  and the normal derivative of  $p$  was set to zero. At the outflow boundary, the normal derivatives of all variables were set to zero.

We specify free boundary conditions along the top of the domain so that there is no boundary dampening of the evolving velocity fields:

$$K_M \frac{\partial u}{\partial z} = u_*^2; \quad \frac{\partial w}{\partial z} = \text{const}; \quad K_E \frac{\partial E}{\partial z} = 0; \quad \frac{\partial El}{\partial z} = kE; \quad \frac{\partial p}{\partial z} = 0.$$

At the bottom:

$$E = \frac{u_*^2}{c_2^{2/3}}; \quad El = kz_0E; \quad \frac{\partial p}{\partial z} = 0,$$

where  $z_0$  is the momentum roughness length. To account for variable upwind and downwind surface roughness values, different values of  $z_0$  were specified over land ( $10^{-1}$  m) and water ( $10^{-4}$  m). Because of the limited size of the waterbodies being studied,  $X_W = 60$  m, and for simplicity, it was specified that  $z_0$  was independent of  $u_*$ , and that  $z_0 = z_{0h} = z_{0q}$ . A no-slip condition was imposed for the velocity fields such that  $u = w = 0$ , and the friction velocity was calculated based on the mean velocity above the surface through use of a wall function [29].

3.2.2.2. *Temperature and Humidity Fields.* As we are concerned with the shallow regions of the atmospheric boundary layer, temperature and humidity were considered to be well-mixed over the height of the domain at the upwind boundary. The values used upwind, and at the lower boundary sections corresponding to land, were set to the values of air temperature and specific humidity recorded at the upwind meteorological station. Of course, where the ambient stability departs from neutral, vertical temperature and humidity stratification could be specified directly at the upwind location using profiles described by Monin–Obukhov similarity theory. Indeed, we see later that this is somewhat of a necessity as the application of vertically homogenous profiles is not ideal. Unfortunately, our data were insufficient to explicitly define stability corrected profiles upwind, and so we imposed the well-mixed assumption at the upwind boundary as other authors have done (e.g., [30]). Temperature at the bottom boundary grid cells corresponding to the water surface were set to the water surface temperature,  $\theta_s$  ( $^{\circ}K$ ), which was calculated

across the length of the waterbody based on a linear interpolation of data from the three temperature sensors shown in Figure 2. The specific humidity at the water surface,  $q_s$  (kg/kg), was estimated from the surface temperature data using [37]:

$$q_s = 135000 \left[ \exp \left( \frac{-4157}{\theta_s - 33.91} \right) \right]. \quad (19)$$

At the downstream boundary, the normal derivatives of both temperature and humidity were set to zero.

3.2.2.3. *Parameterization of the Shelter.* The influence of shelterbelt density on the evolving wind-field is parameterized within Equations (1), (2), (7) and (8) by the drag coefficient,  $C_D$ , which is related to porosity via a resistance coefficient,  $R$  [15]:

$$R = \int_{-\infty}^{\infty} C_D A dx, \quad (20)$$

where  $A$  is the plant area density of the shelterbelt.  $R$  is a non-linear function of porosity as suggested by Heisler and Dewalle [31].

The different field scenarios depicted in Figure 2 were accommodated within the numerical model as shown in Figure 3. Note that the computational grid of the BO scenario was scaled using  $H_{AB}$ , as  $H_{BO}$  is not quite as clearly defined. Rather than explicitly capturing the bank in both the BO and AB scenarios as an undulation in the bottom boundary (which would unnecessarily complicate the numerics), it was specified that all nodes within the region of the bank had a negligible porosity ( $R = 150$ ). The artificial (fence) windbreak situated on top of the bank for the AB scenario was implemented within the numerical domain by specifying a resistance coefficient equivalent to 30% porosity for two columns of cells ( $0.3H$ ) above the bank. The natural shelter (NS) was considered to be ‘three-dimensional’, so porosity was prescribed to be loose over the trunk region, dense in the mid-region, and loose at the top [32]. Porosity values were based on somewhat qualitative optical estimates taken from photographs, and as the model is averaged laterally, it was assumed to vary only in the  $x$  and  $z$  dimensions. We note that this estimation introduces some uncertainty in the specifications of the resistance coefficient and therefore the predicted wind fields. For example, the WT model indicated that a change from 55% to 44% porosity modified the maximum windspeed reduction,  $\hat{u}_{max}$ , from approximately 0.44 to 0.28, although there was negligible change to the distance downwind where  $\hat{u}_{max}$  occurred [33].

### 3.2.3. Numerical Testing

Before application of the model to the experimental scenarios described above, we verified that our implementation performs as well as expected by simulating flow through a simple, ‘2D’, porous barrier. As done in previous studies [13, 15, 22],

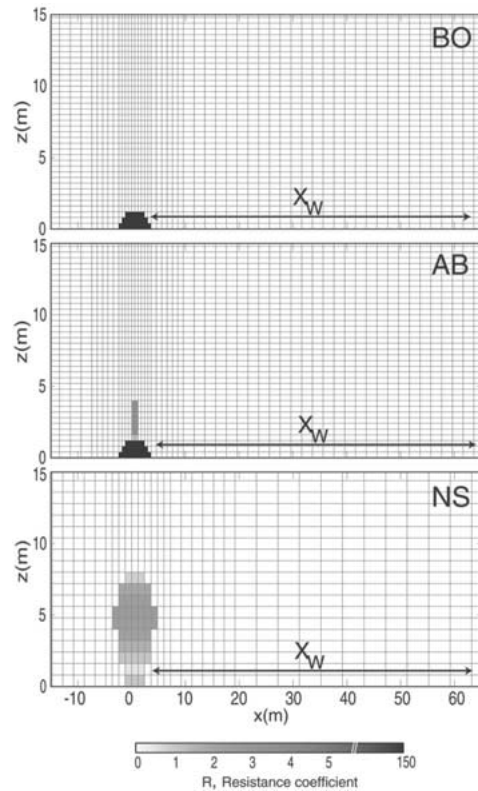


Figure 3. Details of the plaid grid used for the BO (Bank Only), AB (Artificial Barrier) and NS (Natural Shelter, Katanning,  $H = 8$  m) scenarios (only the surface region near the waterbody is shown for clarity). The parameterization of the shelter within the domain for each of the scenarios is indicated by the resistance coefficient shading.

we tested against the experimental data of Bradley and Mulhearn [14]. In this experiment, shear stress and windspeed data were collected under neutrally stratified conditions about a windbreak ( $H = 1.2$  m) aligned perpendicular to the mean flow. As with the other authors, we specified equal upwind and downwind surface roughness values ( $z_0 = 0.002$  m), and used a resistance coefficient of  $R = 2$ . Our simulations confirm that the model predicts the mean wind field to a high degree of accuracy (Figure 4).

Although not shown here, we also tested the model under a range of local advection conditions, including the ‘lagoon advective flow’ scenarios of Wilson *et al.* [22] where an unstable approach flow encounters a cold lagoon, creating an inversion over the surface, and secondly where a stable approach flow encounters a warm lagoon creating an unstable internal boundary layer. The lagoon scenarios are a good test as they are conceptually similar in design and dimension to our BO scenario except for the presence of the earthen bank. We can report that our code performed equally well in simulating the mean properties of the momentum

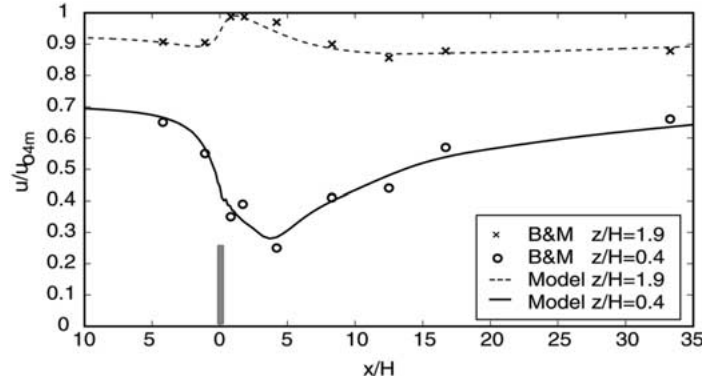


Figure 4. Horizontal windspeed profile comparison between the simulated and B&M (Bradley and Mulhearn, 1983) experimental data for a windbreak of  $H = 1.2$  m,  $z_0 = 0.002$  m and a resistance coefficient,  $R = 2$ . Windspeed data has been normalized by the upstream windspeed at  $z = 4$  m ( $u_{0.4}$  m).

and thermal internal boundary layers (to within  $0.1 \text{ m s}^{-1}$  and  $0.2 \text{ }^\circ\text{C}$  respectively) downwind of the surface discontinuity. This result is encouraging considering our lower order closure scheme and different numerical methods.

### 3.3. MODEL APPLICATION

It is our aim in this analysis to simulate typical summer conditions (when evaporation is highest) with the aerodynamic model and to assess its performance against the field data. To achieve this, two days of reliable field data from each of the Corrigin and Katanning trials were selected, chosen particularly because the direction of the wind was largely perpendicular to the shelterbelt ( $\pm 15^\circ$ ) for the entire period. The chosen simulation periods additionally exhibited ‘typical’ diurnal cycles in the forcing meteorological parameters (temperature, humidity and windspeed), making it possible to individually examine the surface heat flux response to wind-shelter under stable, neutral and unstable conditions.

To compare the simulated momentum, temperature and humidity predictions with those observed in the field (Sections 4.1 and 4.2), stable, neutral and unstable periods were identified in the data based on an estimation of the bulk Richardson Number,  $Ri_B$ :

$$Ri_B = \frac{gz(T_z - T_s)}{T_0 u_z^2}, \quad (21)$$

between the surface and  $z = 0.5$  m above the water. For the purposes of the comparison, surface water temperatures ( $T_s$ ) and upwind values of windspeed, air temperature and specific humidity ( $u_0$ ,  $T_0$  and  $q_0$  respectively) were then used to drive the aerodynamic model for a neutral ( $Ri_B = 0$ ), stable ( $Ri_B \approx 0.3$ ) and unstable ( $Ri_B \approx -0.3$ ) period. Therefore, for each shelter scenario ( $BO$ ,  $AB$  and

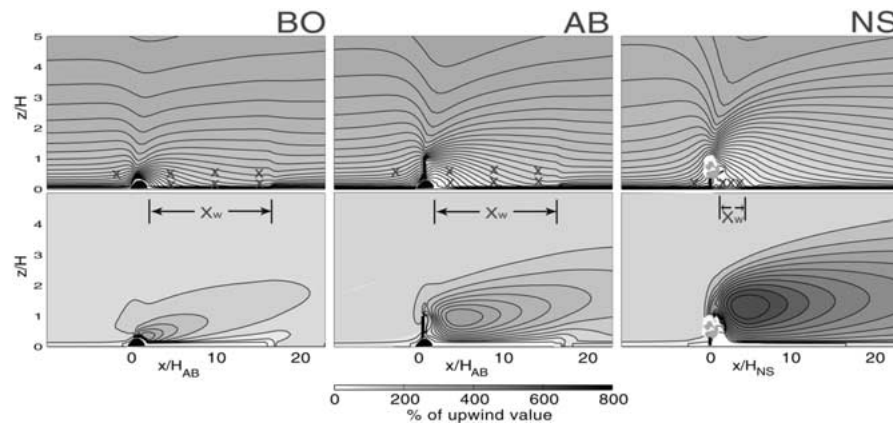


Figure 5a. The velocity deficit,  $u/u_0$  (top, showing approximate anemometer locations) and  $TKE/TKE_0$  (bottom) fields taken from model simulations run under neutral conditions.

*NS*) a ‘typical’ stable, neutral and unstable period was simulated to match the conditions experienced in the field.

Later in the analysis (Section 4.3), the model is used to assess diurnal trends, and so the observed data for each of the Corrigin and Katanning trials was averaged over 3 h periods and used to drive the model. Therefore, for each of the two day comparison periods, 16 simulations were conducted. Finally, the model predictions of evaporation for each of these three-hour simulations were summed over each two day period and compared to the field estimates (Section 4.4).

## 4. Results and Discussion

### 4.1. FLOW FIELDS

Figure 5a is an example of  $u$ -velocity and TKE fields produced by the model under neutral conditions, with the former showing the relative anemometer locations in the experimental setup. On comparison with the field data (Figure 5b), alongwind transects of horizontal windspeed taken from the simulated velocity fields indicate reasonable agreement for all three scenarios, particularly under neutral conditions. However, the simulated momentum fields showed little sensitivity to stability over the water. This is surprising as the TKE fields respond to temperature stratification over the water through inclusion of the buoyancy production term in (7). An inspection of the terms in (7) indicated that the magnitude of the TKE generated by buoyancy production (when  $Ri_B = -0.3$ ) was an order of magnitude smaller than that mechanically generated by the shelter at a height of  $z = 0.5H$ . It is therefore unlikely that inadequate representation of the stratification behind the shelter is responsible for the inaccuracies in the simulated momentum fields.

Closer analysis of the field data presented in Figure 5b, yields an emerging pattern between the velocity deficit and Richardson Number (Figure 6). Although

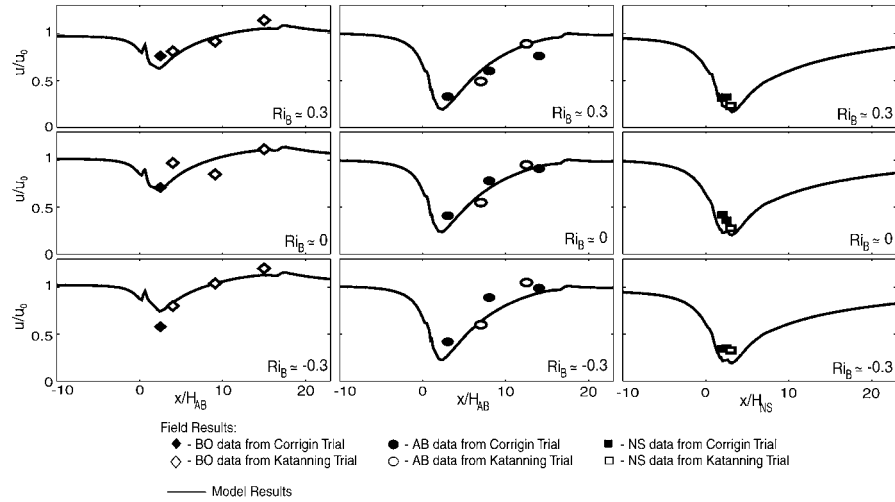


Figure 5b. Alongwind evolution of  $u/u_0$  for stable, neutral and unstable conditions at  $z = 2$  m.

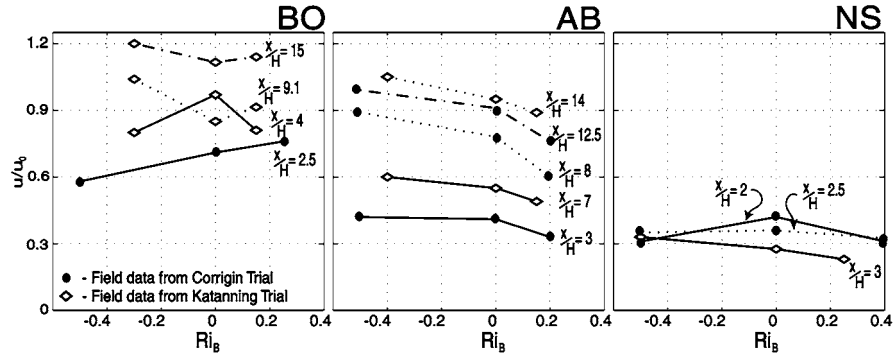


Figure 6. Field data from the three field scenarios ( $z = 0.5$  m) indicating a relationship between the velocity deficit,  $\hat{u} = u/u_0$ , and the Richardson Number for various values of  $x/H$ .

it is not so clear for the BO scenario, the AB and to some extent the NS data show decreasing shelter effectiveness (i.e., increasing  $\hat{u} = u/u_0$ ) as the air over the waterbody becomes increasingly unstable. Similar results have been reported by Seginer [34], who found a pronounced reduction in shelter efficiency during ambient instability over chickpea stubble in Israel.

Furthermore, the field data suggest that the velocity recovery is sensitive to the change in stability,  $\frac{\partial \hat{u}}{\partial Ri}$ , as  $u$ -momentum is more sensitive to stability away from the shelter rather than in the immediate lee where windspeeds are lowest (Figure 7). Seginer [34] found a similar distance dependence and hypothesized that less sensitivity was seen in the near-lee due to a dominance of the shelter-induced

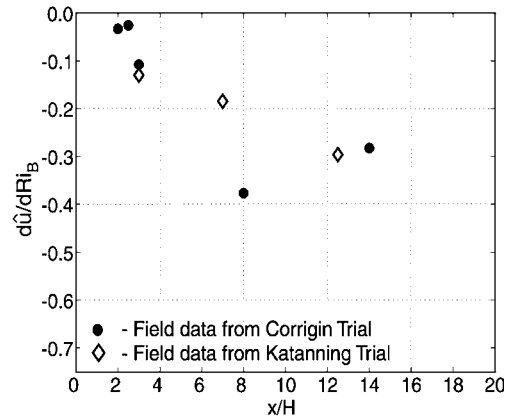


Figure 7. Influence of atmospheric stability on the velocity reduction, ( $\hat{u} = u/u_0$ ), downwind of a shelter. The data points were taken from the AB and NS scenarios only, at a height of  $z = 0.5$  m.

turbulence of the bleed flow. Therefore, despite the deficiencies of the numerical model in capturing this sensitivity, the error is small for waterbodies protected by large shelters (e.g., the NS scenario presented here).

The results of Seginer [34] and their similarity to the field data presented here, motivated us to relax the ‘well-mixed’ assumption at the upwind boundary, and test some hypothetical (but possibly more realistic) stratified approach flow conditions. Accordingly, momentum, temperature and humidity profiles were specified following Monin-Obukhov similarity theory, with the Obukhov length,  $L$ , set to 50 for stable conditions and  $-50$  for unstable conditions. The results qualitatively reflected the trends seen in the field data; increased shelter efficiency during ambient stability, and decreased shelter efficiency during ambient instability. Although we are unable to ascertain whether these non-neutral approach flows occurred during the experiment, this result indicates that perhaps it is not the model creating the inaccuracies, but poor specification of the upwind boundary condition.

#### 4.2. TEMPERATURE AND HUMIDITY FIELDS

In the absence of a shelterbelt or any obstruction to the flow, the transition from land to water modifies the equilibrium flow due to alongwind changes in surface roughness, temperature and humidity. The internal boundary layer (IBL) that develops under local advection has been documented through field trials (e.g., the dryland to moistland stable-IBL data of Bink [36], presented in Wilson *et al.* [22]), numerical solutions to the transport equations (the Rao–Wyngaard–Cote model, [23, 24]) and through application of Monin–Obukhov similarity theory (e.g., [30, 35]). For the case of waterbodies protected by wind-shelters or riparian vegetation, we must consider both the evolving IBL documented in the above studies and the general theory for modification of microclimate by wind-shelters (see Figure 6 of

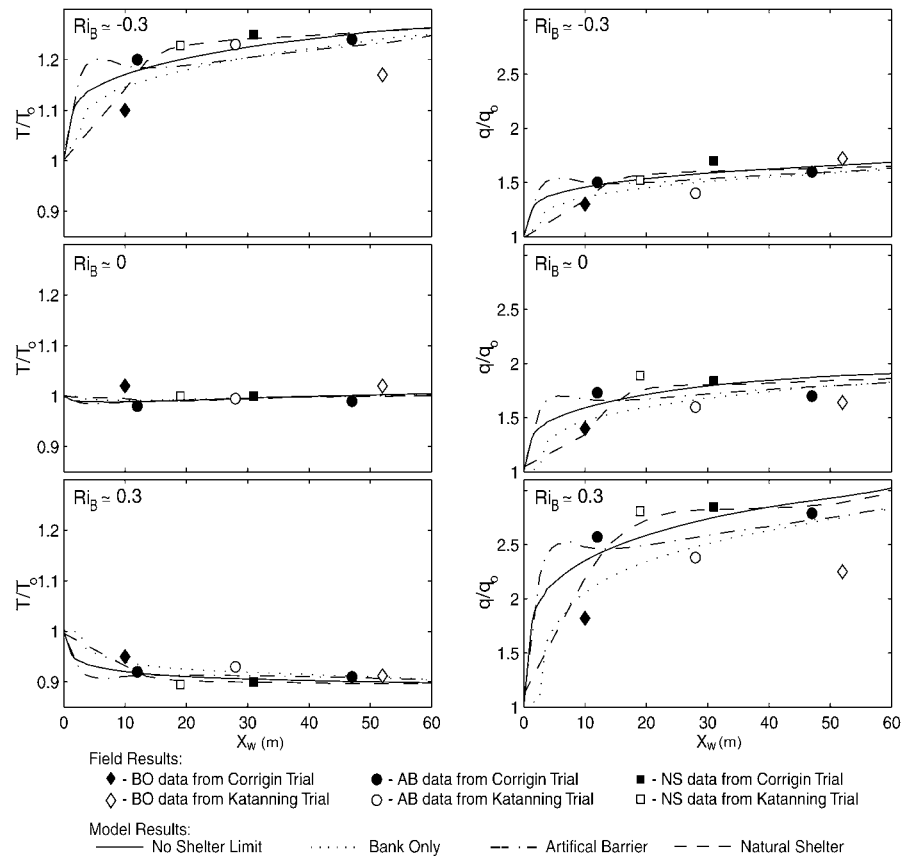


Figure 8. Alongwind variation of temperature (left, in  $^{\circ}\text{C}$ ) and humidity (right) above the waterbody ( $z = 0.5$  m) relative to their upwind values for unstable, neutral and stable conditions. The model simulations (lines) consist of the three scenarios described previously (BO, AB and NS) and an additional simulation conducted in the absence of a shelterbelt (the no-shelter limit). Field data is presented for both the Corrigin (filled points) and Katanning (open points) trials.

[6]); the roughly parabolic temperature and moisture IBL solutions are distorted by scaling with a factor greater than one in the quiet zone and by a factor between zero and one in the wake zone. Both model simulations and field data support this hypothesis for scenarios AB and NS (Figure 8). To facilitate the comparison, the modified microclimates are shown alongside the IBL solution where a smooth transition exists from land to water (i.e., the ‘no-shelter limit’).

The alongwind evolution of temperature and humidity fields for the no-shelter limit is consistent with IBL development discussed previously. The BO scenario shows a similar pattern, however, it is shifted downwind approximately 3 m as a result of the earthen embankment providing a small sheltered region that delays acceleration of air over the water. Further downwind, enhanced turbulence induced

by the embankment reduces accumulation of heat and moisture relative to the IBL solution. This is reflected in the field data, which indicates the least accumulation of heat and moisture of all the scenarios.

Model simulations for the AB scenario show an initial rise in heat and moisture relative to the IBL solution between 0 and 10 m, which then decrease below the IBL prediction with increasing distance downwind. This pattern is reflected in the field data, although the relative variations (both predicted and measured) are small compared to the magnitude of the temperature or humidity excursion from upwind values. Nonetheless, these results support the conceptual model, as the sensor located at 12.5 m is consistently raised above the IBL solution, and the sensor located at 47 m shows consistently lower values for the various forcing conditions.

The NS simulations show reduced scalar concentrations for the first 10 m, raised concentrations between 10 and 30 m, and slightly reduced concentrations further downwind. However, the initial low concentrations are a result of insufficient numerical resolution, caused primarily because of the large value of  $H$  relative to  $X_W$  for this scenario creating relatively large grid cells over the water surface. The field data do suggest a consistent increase in both temperature and humidity compared to the no-shelter limit, which is generally greater than that predicted by the model.

Relative to the alongwind variation in temperature and humidity across the waterbody, the variability between the different shelter scenarios is small. The low sensitivity is a result of the negative feedback between water temperature and atmospheric scalar values. For example, the decrease in turbulent transport of heat and moisture reduces the gradient between the atmosphere and the water surface, which drives the evaporative and sensible heat fluxes. This results in an increase in the water temperature over non-sheltered conditions, which in turn increases the heat and vapour fluxes from the surface, and so the cycle goes. Furthermore, the reduction of shear stress at the water surface for sheltered waterbodies reduces the momentum available to mix the surface layer, resulting in reduced amounts of cooler water reaching the surface. This is of particular importance during a typical midday period when solar heating strongly stratifies the surface layer of the water column. Although not included within the numerical model, there is a further feedback, as reduction in shear stress at the surface reduces the wave height and hence momentum and scalar roughness lengths. Observations in the field also suggest that significant wave height variability exists along the length of the waterbody as the disturbed boundary layer evolves downwind.

#### 4.3. SURFACE HEAT FLUXES

Using simulated momentum and scalar fields, Equations (13) and (14) were used to estimate sensible and latent heat fluxes along the length of the waterbody for unstable, neutral and stable conditions (Figure 9). The no-shelter limit simulations reflect the evolution of the IBL as the dry air moves over the water surface. During the night, the sensible heat flux is directed out of the waterbody due to the water

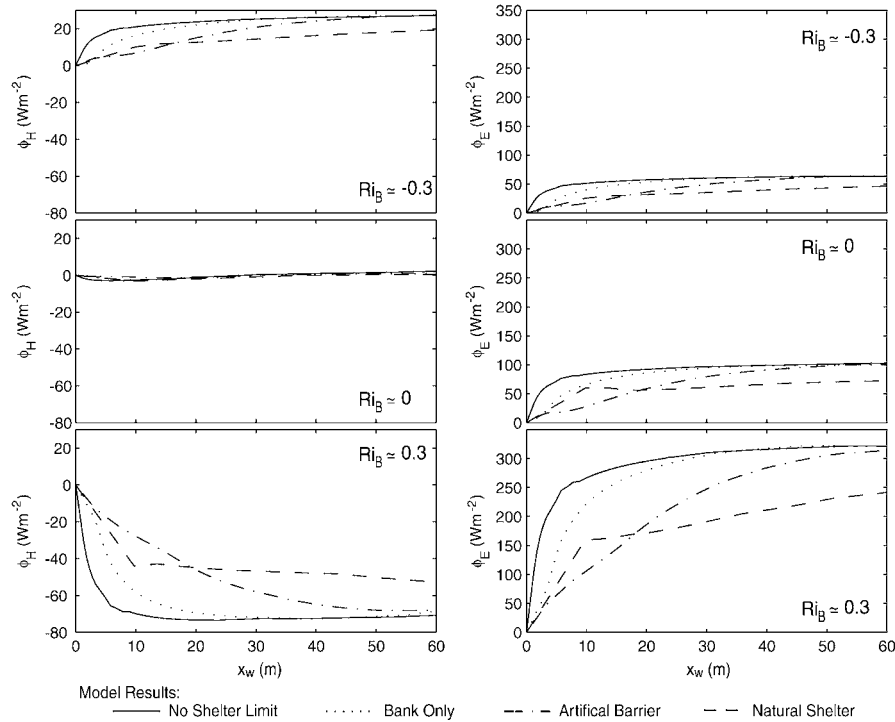


Figure 9. Model predictions of alongwind variation of sensible (left) and latent (right) heat fluxes during unstable (top), neutral (middle) and unstable (bottom) conditions.

being warmer than the air. This convective instability maintains a modest latent heat flux throughout the night despite low wind forcing. In the neutral morning and afternoon periods, sensible heat fluxes are negligible, but higher windspeed and lower atmospheric humidities promote increased latent heat transfer. During the stable midday period, high air temperatures create a positive sensible heat flux into the waterbody, and low atmospheric humidity and high windspeeds result in the highest evaporative heat losses from the water.

The cumulative effects of shelter on the momentum, temperature and humidity fields, and the waterbody, become evident on comparison of the alongwind variation of surface heat fluxes for the different shelter scenarios. The BO waterbodies are similar to their no-shelter counterparts except for a delay in the onset of the boundary-layer. This is predominantly a result of the reduced friction velocity in this region. As suggested by the temperature and moisture accumulation (Figure 8), the impact of the shelter on the alongwind variation of heat fluxes under the AB scenario is more pronounced and extends over most of the waterbody. In this case, the barrier and bank together provide a combined shelter height of 4 m, implying a total protected distance of approximately 13H. The NS scenario provides more substantial evaporation reductions over the entire waterbody because the entire water surface lies within 3–5H of the shelter, and is therefore entirely within the quiet

zone. Over the first 10 m of water however, the natural shelter was less efficient at reducing heat fluxes than the AB protected waterbodies. This resulted from a combination of three reasons: First, as the numerical grid is scaled according to shelterbelt height, adequate solution of the disturbed flow necessitated an excessive domain relative to the size of the waterbody, resulting in poor grid resolution at the scale of interest. Second, the natural shelter was of a higher porosity than the engineered shelter despite its larger size in both the  $x$  and  $z$  dimensions (typically dense shelters provide better reductions in the immediate lee at the cost of increased turbulence and quicker velocity recovery). Third, the shelter was parameterized in a 3D fashion such that less resistance was specified within the near-ground region, promoting preferential bleed flow near the surface, and raising the friction velocity over the nearshore region.

Figure 10 shows three-hour integrations of the forcing meteorology and areally-averaged heat flux predictions from the model for two days of both the Corrigin and Katanning trials. The diurnal trends for each of the shelter scenarios are similar across the range of forcing conditions as was suggested by the similarity seen in the alongwind variation of the heat fluxes, implying that the influence of the wind-shelters is mostly constant relative to the no-shelter limit. This was to be expected based on the scaling behaviour seen throughout the literature on shelterbelt aerodynamics (for example,  $\hat{u}(x) \neq f(u_0)$ ). Where this trend fails to hold, it is attributable to different water surface temperatures between the scenarios modifying the bottom boundary condition. It is interesting to note here that the water temperature of the BO scenario is typically lower for both the Corrigin and Katanning trials (Figure 10). We cannot confirm whether this is in fact because of the higher heat fluxes that result from the lower level of shelter, or whether it is due to some other process (e.g., differences in extinction coefficients or surface area-volume ratios between the waterbodies).

#### 4.4. SHELTER EFFECTS ON EVAPORATION

Integration of the alongwind latent heat flux profile across the length and breadth of the water surface, and over the diurnal cycle shown in Figure 10, provides equivalent mass flux values corresponding to those estimated by the water balance measurements collected as part of the field trial (Figure 11). These daily totals of the mass flux indicate good agreement between the model predictions and the field estimates. In general, the model slightly over predicted the evaporation reduction that the shelters provided as the modelled evaporation was lower than the observed data for eight of the twelve points. It is suspected that this resulted from errors in the estimation of the friction velocity in the nearshore region. This is where both the disturbed wind profile and the change in surface roughness impact heavily on the horizontal variation of  $u_*$ . Nonetheless, considering that we have not concerned ourselves with roughness height variation with windspeed, in addition to the 2D

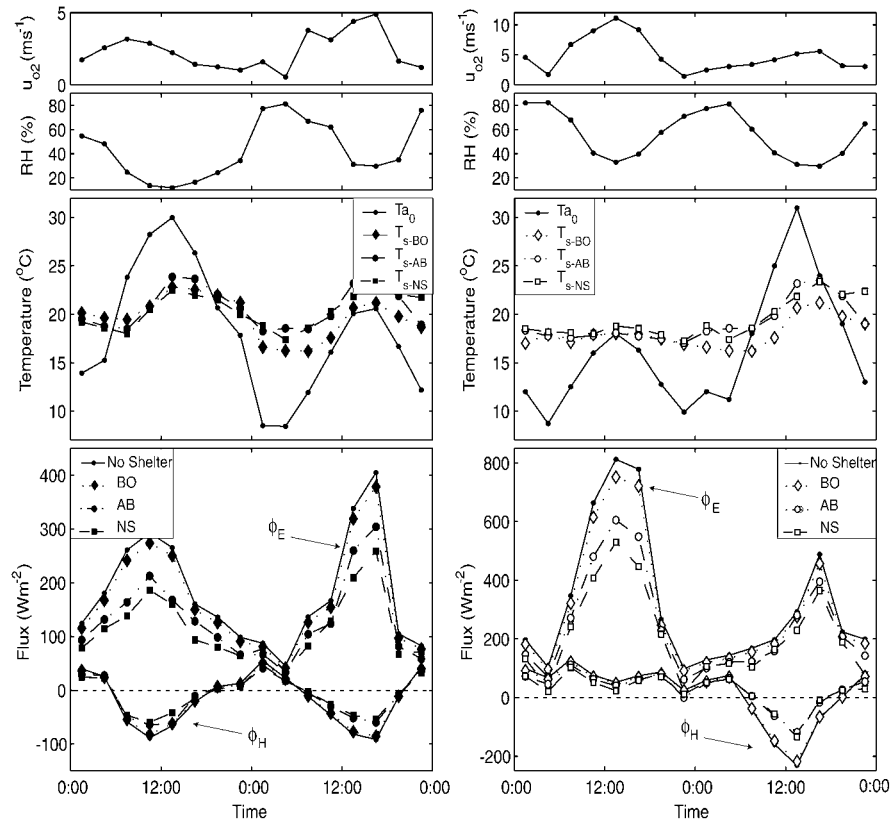


Figure 10. Three-hourly integrations of simulated sensible and latent heat fluxes for a two-day period during the Corrigin trial (left, 14–15th November 2000) and Katanning trial (right, 27–28th November 2000). The corresponding forcing meteorology (air temperature,  $T_a$ , relative humidity,  $RH$ , upwind windspeed,  $u_0$ , and the surface water temperature,  $T_s$ , taken from the central water temperature sensor for each of the three scenarios) is shown in the plots above.

approximation and the complexity of the experimental sites being simulated, this result is encouraging.

Finally, we compare the ability of the different shelter scenarios in reducing evaporation (Table II). Although there was no field trial on a reservoir with no-shelter, the results are presented relative to the model predictions of the no-shelter limit, so that it may act as a control for comparative purposes. The observed data indicate that the presence of the bank resulted in an evaporation reduction over the two days equivalent to 5.8% (0.4 and 11.2% for Corrigin and Katanning respectively). This is supported by anecdotal evidence from land management agencies in Western Australia who promote high dam banks for their wind-sheltering benefits. The model results are similar to the observed data and show more consistency between the trials (6.7 and 7.1% for Corrigin and Katanning respectively). In-

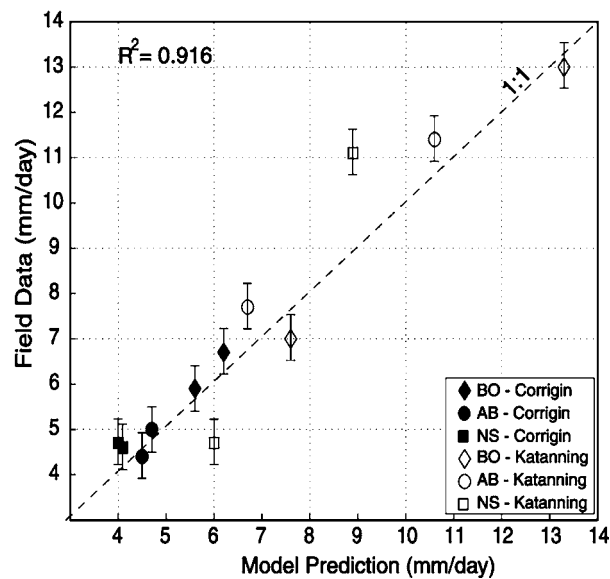


Figure 11. Comparison of areally and diurnally averaged evaporation estimates from the water-balance data and model simulations for the three scenarios. Each point refers to the two-day period for the Corrigin (solid points, 14–15th November 2000) or Katanning (open points, 27–28th November 2000) trial.

cluding the fence windbreak on top of the bank significantly reduced the water losses. Both the Corrigin field and model results for the AB scenario indicated further reductions in excess of 20%. The Katanning field results were less convincing, but still indicated a modest reduction. Evaporation reductions of the NS waterbodies relative to the no-shelter simulations range between 27 and 36%, an encouraging result indeed. With the exception of the Katanning BO scenario, evaporation values predicted by the model were lower than that observed in the field. This is particularly noticeable for the NS scenario. Nonetheless, from a water conservation perspective we conclude that both the artificially constructed and natural shelterbelts have the potential to appreciably reduce evaporation.

The differing efficiencies of the artificial and natural shelterbelts primarily results from their different heights, and therefore the surface area of the waterbody situated within the quiet zone. Although possible, it would not be practical to construct a, say 10 m, high fence shelterbelt around a small agricultural reservoir, where one could instead construct a network of smaller shelterbelts parallel to each other, i.e., one situated upwind of the shoreline, and one or two situated over the water itself. The fence windbreak does come at an increased financial cost compared to a natural shelter, but it is effective immediately (as opposed to waiting for the trees of the natural shelter to mature), and there is no complication with trees competing for the water stored in the reservoir. Natural shelters however, have other advantages in arid agricultural environments such as their relative cost-

*Table 2.* Evaporation estimates (*mm*) from the numerical model and water-balance data for each shelter scenario. Evaporation values are the cumulative value for the two days presented in Figure 10. Percentage values of the BO, AB and NS scenarios relative to the no-shelter simulations are shown alongside to give an indication of the relative efficiencies of the different shelter types.

Scenario	Corrigin (14–15th Nov 2000)		Katanning (27–28th Nov 2000)	
	Model	Field	Model	Field
No Shelter	12.7	N/A	22.5	N/A
BO	11.9 (93.3%)	12.6 (99.6%)	20.9 (92.9%)	20.0 (88.8%)
AB	9.2 (72.7%)	9.5 (74.6%)	17.4 (77.3%)	19.2 (85.1%)
NS	8.1 (64.1%)	9.3 (72.8%)	14.9 (66.2%)	15.8 (70.3%)

effectiveness and reduced maintenance requirements, but also indirect advantages such as providing shade for livestock, increasing biodiversity and reducing rising water tables.

## 5. Conclusion

Our aim has been to investigate the potential use of wind-shelters as tools capable of reducing evaporation from small, agricultural water-supply reservoirs. The role that wind-shelters play on the downwind aerodynamics and microclimate is not straightforward or even well understood, and so we were motivated to develop a numerical code capable of simulating the disturbed aerodynamics and microclimate over the waterbody. The model predictions of the wind field and microclimate over the sheltered waterbodies were validated against data collected as part of a comprehensive field trial.

The model is similar to the shelterbelt turbulent flow model of Wang and Take [15], and was extended to accommodate the presence of a waterbody downwind of the shelter. Additionally, the model solves the evolving temperature and moisture fields in the lee of the shelter, and uses these to estimate the heat fluxes from the water surface. Comparison of model simulations with experimental results indicated that the model performed well in simulating the momentum, temperature and humidity fields.

In particular, the model accurately captured the velocity deficit curve downwind of various ‘three-dimensional’ shelters during neutral conditions, but underestimated the role that atmospheric stability played on the velocity recovery during non-neutral conditions. The field data suggested that there are not only increased shelter effects with increasing atmospheric stability, but also that the relationship between the velocity deficit and atmospheric stability shows significant alongwind variation over the waterbody. Simulations conducted with hypothetical non-neutral approach flow conditions qualitatively reproduced the trend seen in the field data,

implying that horizontal gradients in stratification created by the presence of the waterbody, played little role in the overall evolution of the disturbed momentum fields. Our upwind data was insufficient to confirm whether or not the hypothetical upwind profiles reflected the actual forcing conditions at the time. It is recommended that modelling the impact of non-neutral stabilities on shelter efficiency be further investigated.

Despite the shortcoming of our simulations in this regard, the development of the temperature and moisture fields were well simulated because their evolution was dominated by turbulence generated by the shelter, and not by that generated by non-neutral stabilities. Although the relative impacts of the shelter on the downwind scalar fields were seemingly small, increased accumulation of moisture and heat in the near-lee were seen as persistent features in both the model simulations and field data. In accordance with the conceptual model of McNaughton [6], reduced accumulation was seen further downwind owing to increased turbulent transport and recovering mean horizontal velocities in this region. The net result of the disturbed momentum and scalar fields on the surface heat fluxes was considerable, particularly since the humidity and temperature fields were only modestly affected. It is therefore concluded that the reduced mean wind speeds and reduced turbulent intensities in the near lee were mostly responsible for the reduction in the magnitude of the surface heat fluxes over the water. Areal and diurnally averaged estimates of the evaporative mass flux compared well with water-balance measurements for the various scenarios.

The motivation and focus of this study has been on understanding the effect of wind-shelters on evaporation from agricultural water-supply reservoirs from a water conservation perspective. Accordingly, we report that the evaporation reduction provided by the various wind-shelters improved with increasing shelter effectiveness. Relative to the no-shelter limit (i.e., smooth transition from land to water), the presence of an earthen bank has the potential to reduce evaporation by approximately 6%. Construction of a fence windbreak (30% porosity) on the earthen bank ( $X_w/H = 15$ ) increased the shelter effect over most of the water surface, and resulted in evaporation reductions between 15 and 25%. Waterbodies situated downwind of large natural shelterbelts ( $X_w/H < 7.5$ ) showed marked reductions in evaporation, with observed data indicating reductions of approximately 28% relative to the case without any sheltering. Although our results are specific to these small agricultural reservoirs, the model is capable of simulating evaporative and sensible heat fluxes from a variety of wetlands and small lakes protected by fringing vegetation, providing that sufficient information exists to accurately specify the boundary conditions.

The numerical model presented is a valid tool for understanding the shelter-effect on evaporation from small waterbodies, and allows for estimation of shelterbelt design parameters to optimize the potential evaporation reduction. However, its complicated nature and long run times mean that there is a need for a simple evaporation model capable of parameterizing the influence of wind-shelter on the

evolving boundary layer. Such a tool would be useful for seasonal investigations where wind direction is no longer constant and for coupling with waterbody models for water-balance or hydrodynamic investigations. In a subsequent paper, we parameterize the influence of a wind-shelter on evaporation and include this in a simple Dalton style evaporation model.

## 6. Acknowledgements

The authors wish to acknowledge the Water Corporation of Western Australia and Office of Water Regulation for financial support. In addition, we would like to thank Agriculture Western Australia for support and allowing our experimental work on their Katanning Research Station. Special thanks also go to Richard Guinness who allowed use of his dams for the Corrigin field trial. The authors are grateful to Keith McNaughton and Helen Cleugh for their helpful comments, and the two anonymous reviewers who significantly improved this paper. Centre for Water Research reference *ED1767MH*.

## References

1. Rosenberg, N.J.: 1966, Microclimate, air mixing and physiological regulation of transpiration as influenced by wind shelter in an irrigated bean field, *Agric. Meteorol.* **3**, 197–224.
2. Brown, K.W. and Rosenberg, N.J.: 1971, Shelter-effects on microclimate, growth and water use by irrigated sugar beets in the great plains, *Agric. Meteorol.* **9**, 241–263.
3. Lomas, J. and Schlesinger, E.: 1971, 'The influence of a windbreak on evaporation', *Agric. Meteorol.* **8**, 107–115.
4. Skidmore, E.L. and Hagen, L.J.: 1970, Evaporation in sheltered areas as influenced by windbreak porosity, *Agric. Meteorol.* **7**, 363–374.
5. Messing, I., Afors, M., Radkvist, K. and Lewan, E.: 1998, Influence of shelterbelt type on potential evaporation in an arid environment, *Arid Soil Res. Rehab.* **12**, 123–138.
6. McNaughton, K.G.: 1988, Effects of windbreaks on turbulent transport and microclimate, *Agric. Ecosyst. Environ.* **22/23**, 17–39.
7. Cleugh, H.A. and Hughes, D.E.: 2002, The impact of shelter on crop microclimates: A synthesis of results from wind tunnel and field experiments, *Aust. J. Exp. Agric.* **42**, 679–701.
8. Prueger, J.H., Sauer, T.J. and Hatfield, J.L.: 1998, Turbulence flux estimates of sensible and latent heat near shelterbelts during low wind conditions, *Trans. ASAE* **41**, 1643–1650.
9. Skidmore, E.L., Jacobs, H.S. and Hagen, L.J.: 1972, Microclimate modification by slat-fence windbreaks, *Agron. J.* **64**, 160–162.
10. Brenner, A.J., Jarvis, P.G. and van den Beldt, R.J.: 1995, Windbreak-crop interactions in the Sahel. 2. Growth response of millet in shelter, *Agric. For. Meteorol.* **75**, 235–262.
11. Durst, F. and Rastogi, A.K.: 1980, Turbulent flow over two dimensional fences. In: F. Durst, R. Friedrich, Launder, F.W. Schmidt, U. Schumann and J.H. Whitelaw (eds.), *Turbulent Shear Flows 2*, Springer-Verlag, Berlin, pp. 218–232.
12. Hagen, L.J., Skidmore, E.L., Miller, P.L., Kipp, J.E.: 1981, Simulation of effect of wind barriers on airflow, *Trans. ASAE* **24**, 1002–1008.
13. Wilson, J.D.: 1985, Numerical studies of flow through a windbreak, *J. Wind Eng. Indust. Aero.* **21**, 119–154.
14. Bradley, E.F. and Mulhearn, P.J.: 1983, Development of velocity and shear stress distributions in the wake of a porous shelter fence, *J. Wind Eng. Ind. Aero.* **15**, 145–156.

15. Wang, H. and Takle, E.S.: 1995a, A numerical simulation of boundary-layer flow near shelterbelts, *Boundary-Layer Meteorol.* **75**, 141–173.
16. Whitaker, S.: 1973, The transport equations for a multi-phase system, *Chem. Eng. Sci.* **28**, 139–147.
17. Wang, H. and Takle, E.S.: 1995b, Boundary-layer flow and turbulence near porous obstacles, I. Derivation of a general equation set for a porous medium, *Boundary-Layer Meteorol.* **74**, 73–88.
18. Wilson, J.D. and Mooney, C.J.: 1997, Comments on A numerical simulation of boundary-layer flow near shelterbelts by H. Wang and E. Takle, *Boundary-Layer Meteorol.* **85**, 137–149.
19. Takle, E.S. and Wang, H.: 1997, Reply to comments by J.D. Wilson and C.J. Mooney on A numerical simulation of boundary-layer flow near shelterbelts, *Boundary-Layer Meteorol.* **85**, 151–159.
20. Patton, E.G., Shaw, R.H., Judd, M.J. and Raupach, M.R.: 1998, Large-eddy simulation of windbreak flow, *Boundary-Layer Meteorol.* **87**, 275–306.
21. Wang, H. and Takle, E.S.: 1996, Modeling the evapotranspiration and energy partition of inhomogenous agroecosystems. In: *22nd Conference on Agricultural and Forest Meteorology with Symposium on Fire and Forest Meteorology*, Atlanta, GA.
22. Wilson, J.D., Flesch, T.K. and Harper, L.A.: 2001, Micro-meteorological methods for estimating surface exchange with a disturbed windflow, *Agric. For. Meteorol.* **107**, 207–225.
23. Rao, K.S., Wyngaard, J.C. and Cote, O.R.: 1974a, Local advection of momentum, heat and moisture in micrometeorology, *Boundary-Layer Meteorol.* **7**, 331–348.
24. Rao, K.S., Wyngaard, J.C. and Cote, O.R.: 1974b, The structure of the two-dimensional internal boundary layer over a sudden change of surface roughness, *J. Atmos. Sci.* **31**, 738–746.
25. Wang, H., Takle, E.S. and Shen, J.: 2001, Shelterbelts and windbreaks: Mathematical modeling and computer simulations of turbulent flows, *Annu. Rev. Fluid Mech.* **33**, 549–586.
26. Mellor, G.L. and Yamada, T.: 1982, Development of a turbulence closure model for geophysical fluid problems, *Rev. Geophys. Space Phys.* **20**, 851–875.
27. Yamada, T.: 1982, A numerical model study of turbulent airflow in and above a forest canopy, *J. Meteorol. Soc. Japan* **60**, 439–454.
28. Chorin, A.J.: 1968, Numerical solution of the Navier–Stokes equations, *Math. Comp.* **23**, 341–354.
29. Taylor, P.A. and Delage, Y.: 1971, A note on finite-difference schemes for the surface and planetary boundary layers, *Boundary-Layer Meteorol.* **2**, 108–121.
30. Condie, S.A. and Webster, I.T.: 1997, The influence of wind stress, temperature and humidity gradients on evaporation from reservoirs, *Water Resour. Res.* **33**, 2813–2822.
31. Heisler, G.M. and Dewalle, D.R.: 1988, Effects of windbreak structure on windflow, *Agric. Ecosyst. Environ.* **22/23**, 41–69.
32. Zhou, X.H., Brandle, J.R., Takle, E.S. and Mize, C.W.: 2002, Estimation of the three-dimensional aerodynamic structure of a green ash shelterbelt, *Agric. For. Meteorol.* **111**, 93–108.
33. Wang, H. and Takle, E.S.: 1997, Momentum budget and shelter mechanism of boundary-layer flow near a shelterbelt, *Boundary-Layer Meteorol.* **82**, 417–435.
34. Seginer, I.: 1975, Atmospheric-stability effect on windbreak shelter and drag, *Boundary-Layer Meteorol.* **8**, 383–400.
35. Weisman, R.N. and Brutsaert, W.: 1973, Evaporation and cooling of a lake under unstable atmospheric conditions, *Water Resour. Res.* **9**, 1242–1257.
36. Bink, N.J.: 1996, *The Structure of the Atmospheric Surface Layer Subject to Local Advection*, Ph.D. Thesis, Wageningen Agricultural University, 206 pp. ISBN 90-5485-513-4.
37. Glanz, D.J. and Orlob, G.T.: 1973, *Lincoln Lake Ecologic Study*, Report DACW27-73-C-0064, Water Resour. Eng. Inc., Walnut Creek, CA.